REFERENCE COPY

[redacted]

UNCLASSIFIED

NATIONAL AERONAUTICS AND SPACE ADMINISTRATION

Space Programs Summary No. 37-37, Volume II

for the period November 30, 1965 to December 31, 1965

The Planetary–Interplanetary Program

(Title Unclassified)

LAB-C00449

JET PROPULSION LABORATORY
LIBRARY
MAR 8 1966
CALIFORNIA INSTITUTE OF TECHNOLOGY

482
Copy No.

Classification Changed to UNCLASSIFIED
JPL-Letter 4 Authority NASA-Langley
on Nov. 4, 1970 signed by W. E. Hall
Date Jan. 4, 1971 By Q. Pastrain

JET PROPULSION LABORATORY
CALIFORNIA INSTITUTE OF TECHNOLOGY
PASADENA, CALIFORNIA

January 31, 1966

[redacted]

GROUP 4 Down... ...decl... ...interval; ...declassified after 12 ye...

UNCLASSIFIED

145336

Preface

The *Space Programs Summary* is a six-volume, bimonthly publication that documents the current project activities and supporting research and advanced development efforts conducted or managed by JPL for the NASA space exploration programs. The titles of all volumes of the *Space Programs Summary* are:

Vol. I. The Lunar Program (Confidential)

Vol. II. The Planetary–Interplanetary Program (Confidential)

Vol. III. The Deep Space Network (Unclassified)

Vol. IV. Supporting Research and Advanced Development (Unclassified)

Vol. V. Supporting Research and Advanced Development (Confidential)

Vol. VI. Space Exploration Programs and Space Sciences (Unclassified)

The *Space Programs Summary,* Vol. VI consists of an unclassified digest of appropriate material from Vols. I, II, and III; an original presentation of technical supporting activities, including engineering development of environmental-test facilities, and quality assurance and reliability; and a reprint of the space science instrumentation studies of Vols. I and II.

W. H. Pickering

W. H. Pickering, *Director*
Jet Propulsion Laboratory

Space Programs Summary No. 37-37, Volume II

Copyright © 1966, Jet Propulsion Laboratory, California Institute of Technology

Prepared under Contract No. NAS 7-100, National Aeronautics & Space Administration

This document contains information affecting the national defense of the United [redacted] 794, the transmission [redacted] to an unauthorized person [redacted]

[redacted] UNCLASSIFIED

Contents

I. *Mariner* Project 1
A. *Mariner* Mars 1964 1
B. *Mariner* Venus 1967 2
C. Telecommunications: *Mariner C* Command Subsystem 2

II. *Voyager* Project 6
A. Introduction 6
B. Guidance and Control 7
C. Propulsion 19
References 22

III. Future Projects 24
A. Introduction 24

[redacted] UNCLASSIFIED

UNCLASSIFIED

cannot be demodulated, because the signal level is below the telemetry threshold. On December 1 the total received power was estimated to be −177.7 dbm.

If the *Mariner IV* spacecraft is operating in 1967, an attempt will be made to obtain telemetry. This effort will be carried out while simultaneously tracking the *Mariner* Venus 1967 spacecraft.

B. *Mariner* Venus 1967

The *Mariner* Venus 1967 mission was authorized in late December 1965, and the project is currently getting under way. Current plans call for a single launch in 1967, using the *MC-4* spacecraft (a *Mariner* Mars 1964 flight spare) modified to conform to the 1967 mission requirements, and an *Atlas/Agena* launch vehicle.

C. Telecommunications: *Mariner C* Command Subsystem

1. General Description

The purpose of the overall command subsystem link is to relay information from Earth to the spacecraft. From this information specified spacecraft functions may be controlled. The overall *Mariner C* command link is presented in Fig. 1.

The decision for the transmission of a command to the spacecraft originates at JPL's Space Flight Operations Facility (SFOF). From SFOF the 26-bit command word is sent to the Deep Space Instrumentation Facility (DSIF) by voice and by teletype. The ground command system (GCS) operator at DSIF confirms the command decision and prepares the GCS for the command transmission to the spacecraft. The function of the GCS is to modulate the radio-frequency carrier with a composite command signal to be sent to the spacecraft.

The first step in GCS transmission sequence is to enter the binary-coded command message. This message is usually in the form of a punched paper tape.

The GCS verifies the accuracy of the tape through redundant comparison checks and parity checks. Then the GCS operational readiness capability is checked by performing an internal operational cycle with no output leaving the machine. After the GCS has verified the command message and its own internal operation, the GCS output (the composite command signal) phase modulates the carrier of the ground radio transmitter.

While modulating the RF carrier, the GCS conducts a bit-by-bit comparison which may inhibit transmission at any time. This is a safeguard against false information being transmitted to the spacecraft. Further details of GCS operation are found in *SPS 37-35*, Vol. II.

The function of the spacecraft command subsystem is to demodulate the composite command signal obtained from the spacecraft radio receiver, to decode the command message, and to provide command instructions to designated spacecraft subsystems.

The composite command signal is recovered from the modulated RF carrier by the spacecraft radio receiver. The composite command signal output from the spacecraft radio receiver is the input to the spacecraft command detector. The detector separates the composite command signal into a synchronization channel and a data channel. Within the synchronization channel the bit sync is established. The data channel detects the binary bit stream contained within the composite command signal.

The binary data bit stream is the input to the command decoder. This input is used by the decoder to establish command word synchronization, to decode the command address, and to activate command outputs to the designated spacecraft subsystems.

Further design details of the spacecraft command subsystem are presented in *SPS 37-29*, Vol. VI, pp. 37–39.

2. Acquisition

The composite command signal is comprised of a pseudonoise (PN) synchronization code which is linearly summed with a biphase modulated data subcarrier (Fig. 2a). Before any command bit detection can be accomplished, the replica of the cyclic PN code (PN′) in the spacecraft command detector must be aligned and phase-locked to the PN component of the composite command signal (Fig. 2b). This is accomplished as follows:

(1) The command subcarrier frequency ($2f_s$) in the command modulator is offset slightly from the value

UNCLASSIFIED

I. *Mariner* Project

A. *Mariner* Mars 1964

The early objective of the Planetary–Interplanetary Program was the initial probing of the planets Mars and Venus by unmanned spacecraft. The initial probing of Venus was successfully accomplished by *Mariner II*. The initial probing of Mars was successfully accomplished by *Mariner IV*. The next step in this program is a second probe of Venus by a *Mariner* spacecraft during the 1967 opportunity.

The primary objective of the *Mariner C* mission (*Mariner* Mars 1964 Project) was to conduct closeup (flyby) scientific observations of the planet Mars during the 1964–1965 opportunity and to transmit the results of these observations back to Earth.

A secondary objective was to provide experience and knowledge about the performance of the basic engineering equipment of an attitude-stabilized flyby spacecraft during a long-duration flight in space, farther away from the Sun than the Earth is. An additional secondary objective was to perform certain field and/or particle measurements in interplanetary space and in the vicinity of Mars.

The *Mariner III* (*MC-2*) spacecraft was launched November 5, 1964. The nose cone failed to eject from over the spacecraft, thereby precluding solar panel deployment, among other things; and the battery power was depleted 8 hr and 43 min after launch.

The *Mariner IV* (*MC-3*) spacecraft was successfully launched November 28, 1964 in a Mars encounter orbit about the Sun. The Phase 1 portion of the *Mariner IV* flight was successfully concluded October 1, 1965 when a DC-12 command was transmitted from the 100-kw Venus Station, which resulted in a transfer of the spacecraft transmitter from the high-gain antenna to the low-gain or omniantenna. Phase 2 has been in process since that moment. The DSN will make periodic attempts, approximately one a month, to receive an RF signal from *Mariner IV* in its orbit about the Sun. The earliest significant efforts will probably take place when the new 210-ft dish antenna system at Goldstone is in an R&D operational mode, sometime in the spring of 1966.

On November 1, 1965 the *Mariner IV* RF signal, modulated by telemetry, was received by the Venus Station. The *Mariner IV* signal was again received December 1, 1965, and it was still modulated by telemetry. The carrier

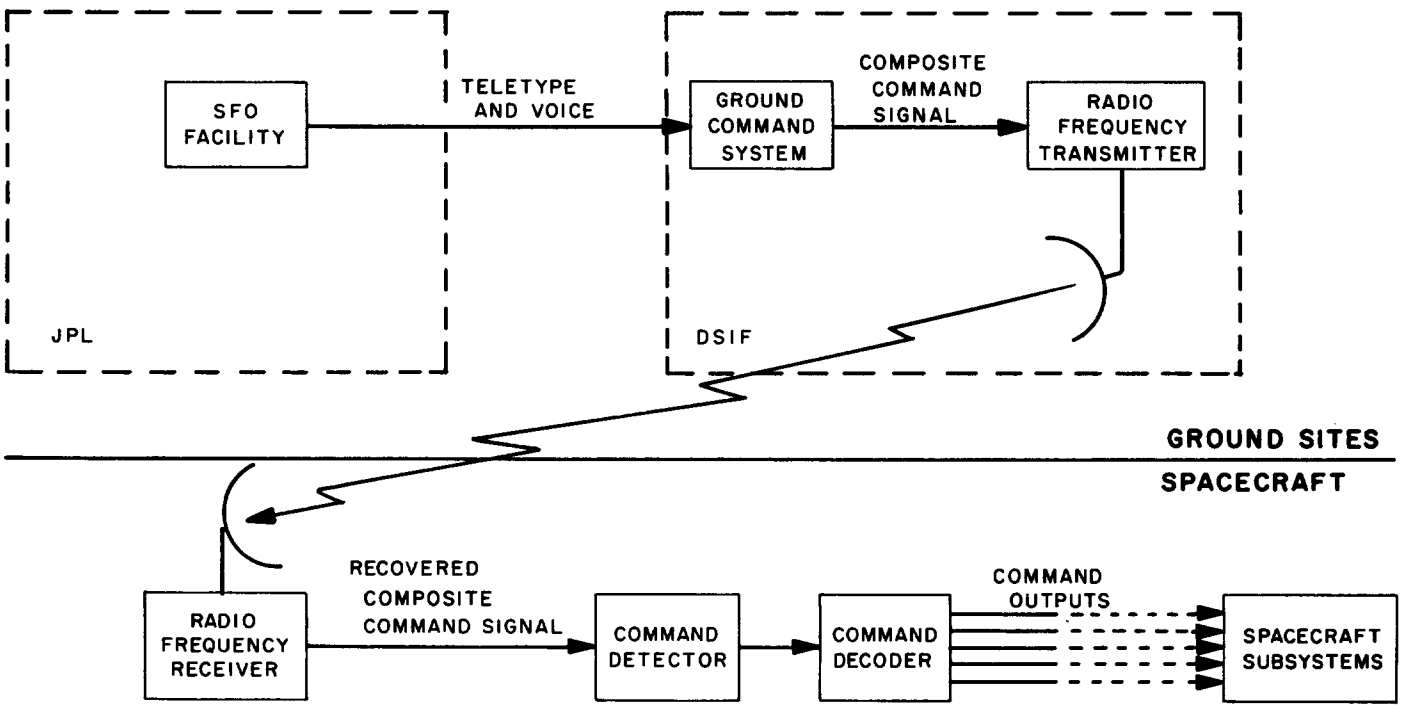

Fig. 1. *Mariner C* command link

of $2f_s'$ received via telemetry from the spacecraft. This causes a gradual precession of the alignment of PN with respect to PN′.

(2) Until PN and PN′ are aligned in phase, the signal at Point K (Fig. 2b) is of a noise-like character. When PN and PN′ become aligned in phase, the $f_s \angle 90°$ component derived from the received synchronization code appears at Point K. This signal is filtered and limited then applied to the phase-locked-loop (PLL) filter. The frequency of the VCO in this loop is initially offset from that of the received signal. If this offset is not too large for the operating bandwidth of the loop, and if the noise component at the time the PN codes become correlated is not unusually large, the loop phase error signal will be sufficient to pull the frequency of the VCO so as to align the phase (and frequency) of $2f_s$ and $2f_s'$. This in turn will hold PN and PN′ in phase alignment. The command detector is then said to be "in-lock," and the command bit detection process can begin.

In this command detector the time required to achieve lock is a function of the following parameters:

(1) The magnitude of the offset of $2f_s$ (GCS) with respect to $2f_s'$ (spacecraft command detector).

(2) The operating bandwidth and dumping factor of the phase-locked-loop (PLL).

(3) The amplitude and distribution of the noise introduced by the radio link.

Increasing the frequency offset ($2f_s - 2f_s'$) results in a relatively rapid precession of PN with respect to PN′. This contributes to more rapid acquisition times, unless the offset is so great that the PLL is unable to respond quickly enough to achieve lock during the brief period when PN and PN′ are aligned.

Widening the PLL bandwidth would allow larger frequency offsets and thus more rapid acquisition times. However, widening the PLL bandwidth eventually allows the level of the noise to become large enough as to inhibit acquisition of lock. Also, the signal-to-noise ratio (SNR) in the loop must be high ($\approx$13.0 db), since it is the source of the phase reference used to demodulate the data subcarrier. Within the *Mariner C* subsystem the loop bandwidth was designed for approximately 2 cps, a compromise between error rate performance and acquisition time. The resultant acquisition time versus frequency offset and SNR are plotted in Fig. 3. During the flight of *Mariner IV*, the subcarrier frequency offset ($2f_s - 2f_s'$) was usually set at $\pm$1.5 cps.

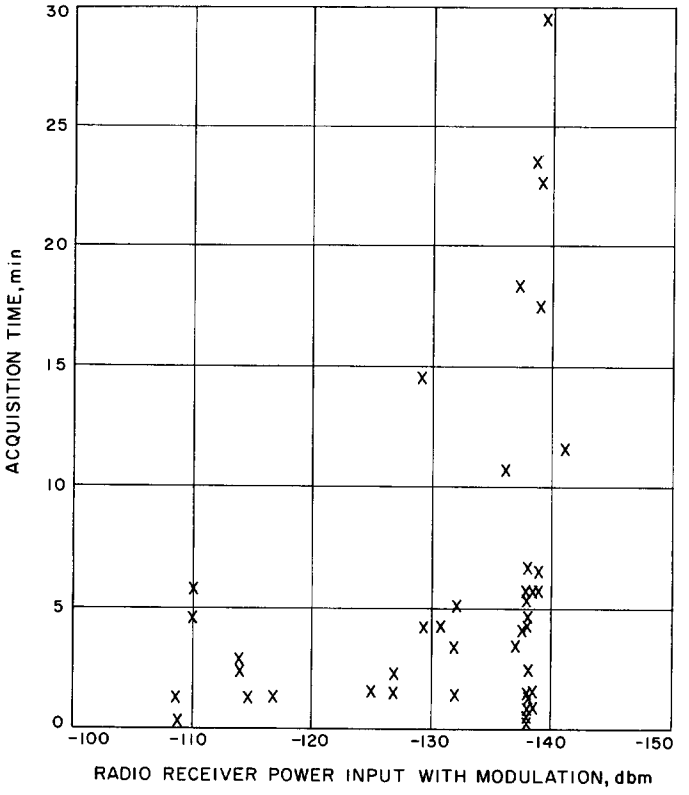

Fig. 4. *Mariner IV* acquisition time

In order to properly evaluate the *Mariner C* probability of error, the *Mariner C* life test command subsystem underwent bit error testing from September 1, 1964 through June 14, 1965. During this time a total of 16,611,840 bits were sent through the command subsystem at a signal-to-noise ratio of 19.5 db. The resulting bit error probability was 3.19×10^{-6}. This represents approximately 6½ months of uninterrupted bit error testing within the error rate design limits.

4. Performance During Mariner IV Mission

Meaningful information about the command bit error rate is not available from *Mariner IV* flight data, due to the very few commands that were sent to the *Mariner* spacecraft. During the entire *Mariner IV* flight, only 85 separate commands (representing 2210 bits) were transmitted. No errors were recorded as all these commands were executed properly.

5. Command Subsystem Reliability

A total of six spacecraft command subsystems were built for the *Mariner C* Project. Upon arrival at JPL each unit was qualified by a JPL flight acceptance test. These units accumulated a total of over 38,860 operating hours after delivery to JPL. Only one equipment failure occurred following completion of JPL flight-acceptance tests. The failure consisted of an intermittent open circuit in an output switch transformer. This failure occurred in the life test command subsystem after 10,800 hr of operation. The effect of this failure was to disable 1 of the 29 direct commands.

Based on the accumulated 38,860 hr of operation (equivalent to 4.5 yr of continuous operation of a subsystem), the mean time between failures is 38,860 hr. It is to be noted that the mean time between failure, based upon predicted component failure rates, was estimated at 15,075 hr.

6. Conclusions

The performance of the spacecraft and ground command subsystems throughout the *Mariner C* project was quite satisfactory. All of the 85 commands transmitted to the spacecraft were executed faultlessly. The final command, transmitted on October 1, 1965, established the present "command distance record" at 191 million miles.

Although the acquisition performance of the *Mariner C* command detector was within specification limits, flight experience indicated that more rapid and more predictable command sync acquisition would be desirable. JPL has begun study of modulation/detection techniques and system implementation which incorporate rapid automatic acquisition with minimal participation required from personnel in the field.

UNCLASSIFIED

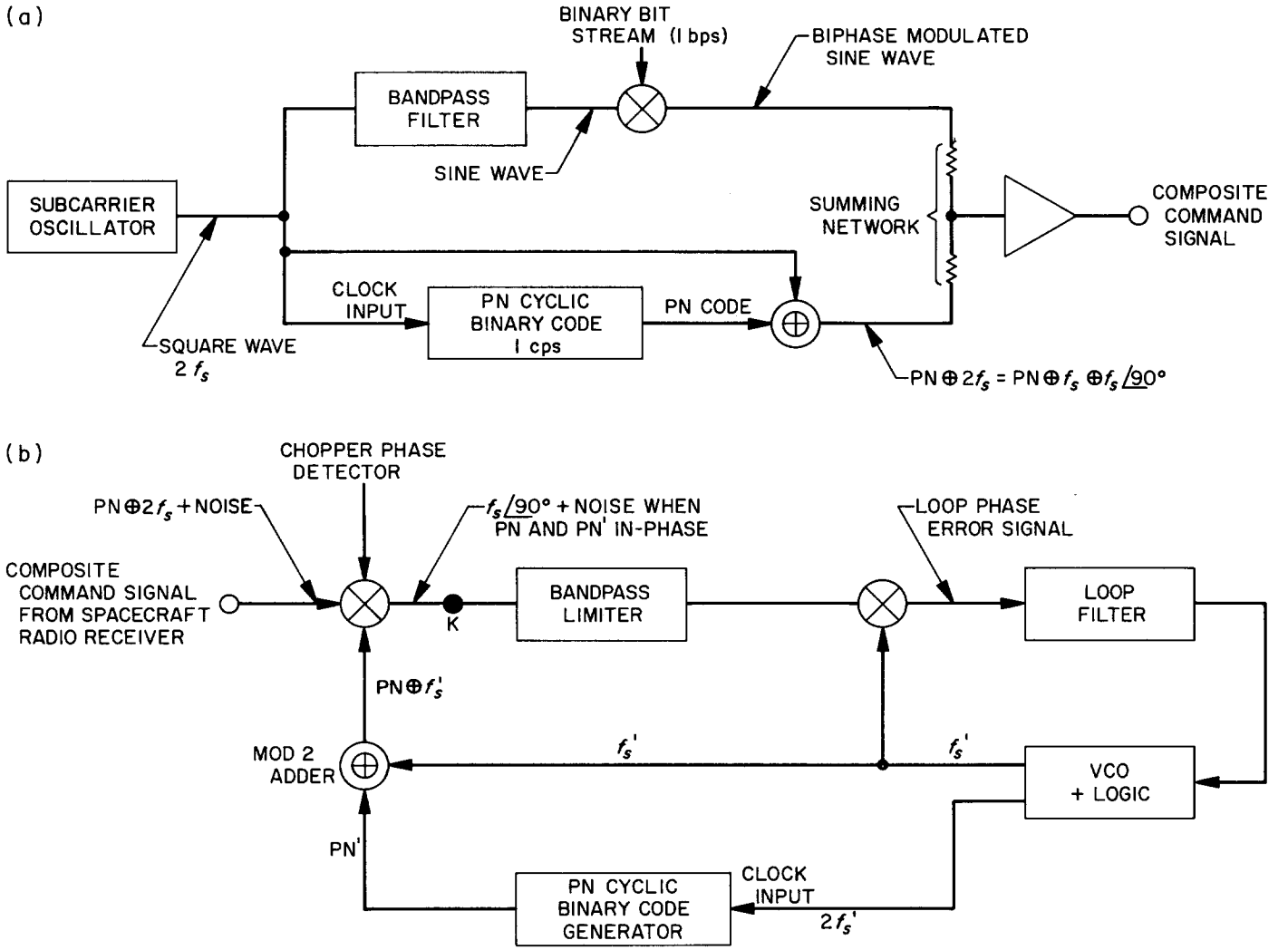

Fig. 2. *Mariner* C command subsystem; (a) command modulator, (b) command detector sync channel

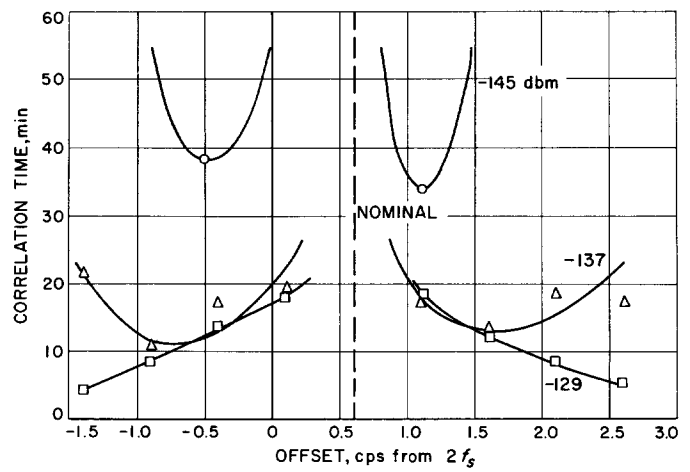

Fig. 3. *Mariner* C life test subsystem correlation time versus offset

The acquisition time as a function of total power input to the radio receiver is plotted in Fig. 4. The dispersion lock time is due partly to the statistics of the operation and partly to imperfect field operations.

3. Command Error Rate Performance

The *Mariner C* PSK-modulated data subcarrier is theoretically capable of producing a bit error rate of $\leq 10^{-5}$ at a normalized SNR of 9.6 db if perfect subcarrier phase reference and bit sync signals are available. In the *Mariner C* command subsystem two-thirds of the total composite command signal power is used to derive the phase reference and bit sync signals. Even with this allocation of power, the phase reference signal contains significant jitter at threshold. As a consequence the overall command subcarrier link bit error rate performance is specified at $\leq 10^{-5}$ at a normalized SNR $\geq 18.5 \pm 1$ db.

UNCLASSIFIED

UNCLASSIFIED [redacted]

II. *Voyager* Project

A. Introduction

1. Objectives

The primary objective of the *Voyager* Project is to carry out scientific investigations of the solar system by instrumented, unmanned spacecraft which will fly by, orbit, and/or land on the planets. Emphasis will be placed on acquisition of scientific information relevant to the origin and evolution of the solar system, the origin, evolution, and nature of planetary life, and the application of this information to an understanding of terrestrial life. The primary objective of the *Voyager* missions to Mars, beginning in 1973, is to obtain information relative to the existence and nature of extraterrestrial life, the atmospheric, surface, and body characteristics of Mars, and the planetary environment by performing unmanned experiments on the surface of, and in orbit about, the planet. A secondary objective is to further our knowledge of the interplanetary medium between the planets Earth and Mars by obtaining scientific and engineering measurements while the spacecraft is in transit.

2. Project Plan

All *Voyager* missions will be conducted as events of an integrated program in which each individual flight forms a part of a logical sequence in an over-all technical plan of both lander and orbital operations. The *Voyager* design will provide for the carrying of large scientific payloads to the planet, the telemetering of a high volume of data back to Earth, and long useful lifetimes in orbit about the planet and/or on the planetary surface. Hardware will be designed to accommodate a variety of spacecraft and/or capsule science payloads, mission profiles, and trajectories. Particular emphasis will be given to simple and conservative design, redundancy wherever appropriate, and a comprehensive program of component, subsystem, and system testing.

Over-all direction and evaluation of the *Voyager* Project is the responsibility of the Office of Space Science and Applications (OSSA) of the National Aeronautics and Space Administration (NASA). Management of the *Voyager* Project and implementation of selected systems is the responsibility of the Jet Propulsion Laboratory (JPL) of the California Institute of Technology (CIT).

3. Technical Description

Two *Voyager* planetary vehicles are to be designed, constructed, and tested for launch on a single *Saturn V* during the 1973 Mars opportunity. Attention is also being given to requirements imposed on such vehicles by launches subsequent to 1973, such as a similar mission planned for 1975. Each planetary vehicle is to consist of a flight spacecraft and a flight capsule, with science experiments conducted in 1973 both from the orbiter and on the planetary surface. The flight spacecraft with its several hundred pounds of science payload will weigh approximately 2500 lb, its retropropulsion subsystem may additionally weigh up to 15,000 lb, and the flight capsule

UNCLASSIFIED [redacted]

will weigh about 3000 lb. The flight spacecraft will be a fully attitude-stabilized device utilizing celestial references for the cruise phase, and will be capable of providing velocity increments for midcourse trajectory corrections and for Mars orbit attainment by both the flight spacecraft and flight capsule. Onboard sequencing and logic will be provided, as well as ground command capability. The flight spacecraft will supply its own power from solar energy or from internal sources and will be capable of maintaining radio communications with Earth. In addition, the flight spacecraft will be thermally integrated and stabilized and will monitor various scientific phenomena near Mars and during transit, and telemeter this information back to Earth; it will also monitor and telemeter data pertaining to spacecraft operation. The flight spacecraft will also provide the flight capsule with services such as power, timing and sequencing, telemetry, and command during the transit portion of the missions and may also serve as a communications relay. The sterilized flight capsule will be designed for separation from the flight spacecraft in orbit, for attaining a Mars impact trajectory, for entry into the Mars atmosphere, descent to the surface, and impact survival, and for surface lifetimes of two days in 1973 and later goals of as much as 6 mo. The flight capsule will contain the power, guidance, control, communications, and data handling systems necessary to complete its mission.

No deep space-flight tests of the flight spacecraft are planned, and compensation by more extensive ground tests will be conducted to the extent possible. The test program for the flight capsule, which is planned to include Earth-entry flight tests will investigate entry, descent, impact, communications, and sterilization.

B. Guidance and Control

1. Mechanization of the Voyager Planet Tracking Approach Guidance Subsystem

a. Introduction. Planet approach guidance requires the measurement of two angles (the Sun-spacecraft-planet angle and the Canopus-spacecraft-planet angle) and the range to the planet as functions of time.

The mechanization presented here as a preliminary recommendation utilizes the existing Sun sensors, Canopus sensor and telemetry system, with the addition of a planet approach tracker to provide the required angle measurements versus time. The required range measurement versus time is derived from radio tracking.

The approach guidance phase proposed for this system consists of 1440 samples of each angle taken at 1-min intervals from two days until one day before closest approach.

A preliminary error analysis gives a performance level, depending on the atmospheric model chosen, of 25- to 65-km 3σ uncertainty of the impact parameter (the distance from the center of the planet to the approach asymptote). This represents a significant improvement over an all-radio tracking performance estimate of 300-km 3σ.

b. The approach guidance phase. The approach guidance problem can be approximated by considering the planet as stationary and the spacecraft as moving along a straight line (the approach asymptote) at a distance b (the impact parameter) from the center of the planet.

Due to the motion of the spacecraft and Mars around the Sun, there is also a spacecraft rotation of about 0.5 deg/day which will be ignored in this simplified model.

If the angle measured at the spacecraft between the center of the planet and the approach asymptote is θ and the distance to the planet from the spacecraft is R, then:

$$\theta R = \text{constant} = b \text{ for } R >> b$$

Since the angle measured by the planet approach tracker, Φ, is based on an arbitrary reference, and differs from θ by a constant, at least two measurements must be taken to allow simultaneous solution for this constant angle C and for b. Additional measurements serve to reduce the uncertainty, caused by random measurement errors, in the determination of b by about the square root of the number of measurements.

Solution of the equations for two measurements gives some insight into optimization of the approach guidance phase.

$$\Phi_1 = \theta_1 + C \qquad \theta_1 = \frac{b}{R_1} \qquad \theta_2 = \frac{b}{R_2}$$

$$\Phi_2 = \theta_2 + C$$

$$\Phi_2 - \Phi_1 = \theta_2 - \theta_1 = \frac{b}{R_2} - \frac{b}{R_1} = \frac{b(R_1 - R_2)}{R_1 R_2}$$

$$b = \frac{R_1 R_2}{R_1 - R_2}(\Phi_2 - \Phi_1)$$

For this simple case, R_2 should be minimized and R_1 maximized to obtain the smallest uncertainty of b.

If a steady drift in Φ is introduced, in addition to the random measurement errors, then R_2 should still be minimized, but there will be an optimum value for R_1. This optimum value for R_1 is a function of R_2 and the relative magnitudes of the random and drift terms. Letting R_2 equal the range at one day before closest approach, which for operational reasons will be the minimum permissible, then for typical values of the random and drift terms the optimum R_1 corresponds to two days before closest approach.

The number of samples to be taken should be selected to reduce the random measurement errors to the same order of magnitude as the fixed and drift terms. For the most optimistic case this requires about 10,000 samples, or a data load of about 4 bits/sec—probably more than will be available for this subsystem.

A compromise value is proposed of 1,440 samples, or one per minute, for the one-day approach guidance phase. Telemetry capacity should permit this data rate of about ½ bit/sec.

c. System mechanization. The spacecraft attitude is not fixed in space, only confined by a limit cycle. Therefore to measure the required angles, the spacecraft motion within this limit cycle must be compensated.

The recommended and simplest method of compensating this motion is to telemeter the error signals of the Sun and Canopus sensors, as well as the angles from the spacecraft axes to the planet center as measured by the planet approach tracker. These five measurements can then be reduced by ground computation to the two required guidance angles.

The other required measurement, planet range versus time, is provided by radio tracking to a much better accuracy then will be possible by on-board measurements during the approach guidance phase. The planet angular diameter can also be telemetered as a backup to this range measurement if desired.

Fig. 1 shows the block diagram for the planet approach guidance system. The items which are unique to this system are the planet approach tracker and the ground computation.

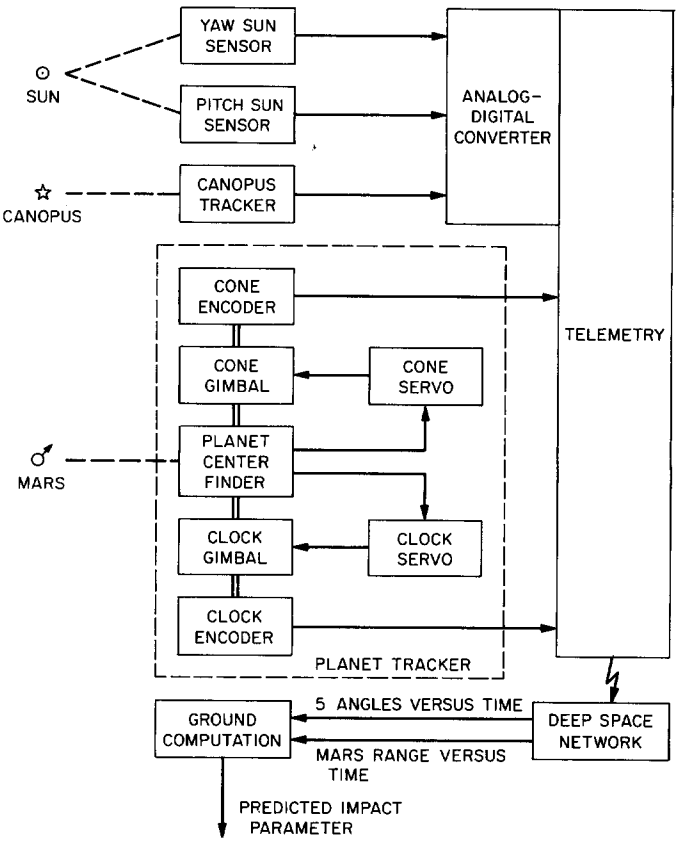

Fig. 1. Planet approach guidance system

The planet approach tracker is composed of a planet center finder, two-axis optical gimballing with digital encoder readout of the gimbal angles, and two-axis servos to maintain the planet center finder at its null position.

The planet center finder utilizes an image dissector as the detecting element. The image dissector has a useful overall field-of-view that is 2 deg in diameter when used with the $f/8$, 16-in. focal length optical system. The instantaneous field-of-view, as determined by the aperture plate, is about 0.02 deg in diameter.

The instantaneous field-of-view is scanned, as shown in Fig. 2, at a low frequency with a semicircular reversing motion upon which a triangular waveform, high-frequency radial scan has been superimposed. The error signal from the high-frequency radial scan is used to servo the radius of the low-frequency semicircular scan so as to track along the sunlit limb of Mars. The sunlit limb of Mars is always maintained in the same orientation on the face of the image dissector by the choice of the cone and clock gimbal system.

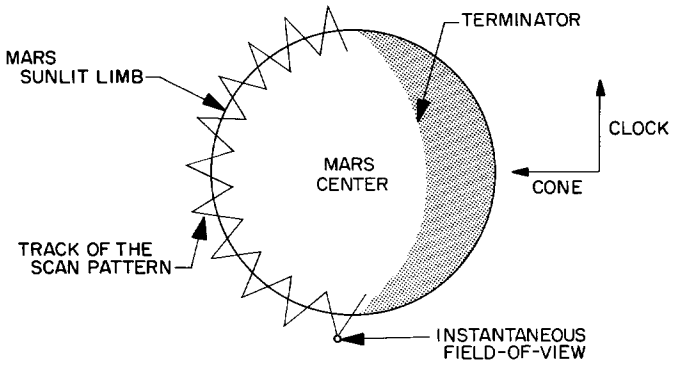

Fig. 2. Planet center finder scan pattern

The radius output signal, derived from the image dissector deflection voltage required to null the high-frequency scan, is then demodulated with respect to the low-frequency scan to provide the cone and clock error signal.

The gimbals are required to provide the ±5 deg of motion that is necessary to accommodate the range of launch and arrival dates and apparent planet motion. The proposed gimbal system used counter-rotating wedges (prisms) mounted in front of the planet center finder. This optical gimbaling mechanization requires no motion of the planet center finder, avoids the deterioration of and the optical perfection required by mirror gimbaling and provides an optical "gear ratio" of about 18 to 1, permitting the use of relatively simple gearing between the encoders, motors, and wedges. This two-axis counter-rotating wedge mechanism will probably require pressurization, but the planet center finder and electronics will not be pressurized.

d. Preliminary error analysis. Table 1 presents a compilation of the sources of uncertainty in the impact parameter for a planet approach guidance system using 1440 samples of each angle taken once per minute between two days and one day before closest approach.

The sources are divided into random (magnitude reduced by the square root of the number of samples), fixed (not reduced at all by multiple samples), pseudo-random (somewhere between random and fixed, depending on conditions), and drifts (similar to random, but with time constants about equal to, or longer than, the approach guidance phase, thus permitting no magnitude reduction by multiple samples).

For this analysis it will be assumed that the motion in the limit cycle combines with the randomly distributed

Table 1. Approach guidance error analysis

	3σ Error magnitude, deg	3σ Average error, deg	3σ Contribution to impact parameter	
			Cone, km	Clock, km
Random				
Sun sensor noise	0	0	0	0
Planet tracker noise	0	0	0	0
Canopus tracker noise	0.015	0.0004	0	4
Fixed				
Uncertainty of true ellipticity			3.5	0
Uncertainty of altitude of apparent Mars limb			6 to 60	6
Pseudorandom				
Calibration of Sun sensors 1% rms	0.03	0.00075	7.5	7.5
Calibration of Canopus sensor 1% rms	0.03	0.00075	0	7.5
Calibration of planet tracker 1% peak	0.02	0.0005	5	5
Quantization of Sun error signal	0.03	0.00075	7.5	7.5
Quantization of Canopus	0.03	0.00075	0	7.5
Quantization of planet tracker	0.005	0.00013	1.3	1.3
Drifts				
Sun sensor	0.001		3	3
Canopus tracker	0.001		0	3
Planet tracker	0.0001		0.3	0.3
Sun sensor power supply 0.1%	0.001		3	3
Telemetry drift	0.001		3	4.2
Mechanical	0.001		3	3
Total 3σ contribution			15 to 60	20
3σ Uncertainty of the impact parameter			25 to 65	

deviations of the calibrated curves from the corresponding true curves to simulate a completely random function that allows reduction of the errors by the square root of the number of samples. In similar manner it will be assumed that the motion in the limit cycle combines with randomly distributed deviations in bit size and location to allow reduction of quantization errors.

Because the precise shape of the curve of planet angles versus range can be computed, it is expected that much larger drift rates can be separated out of the data. However, this is not yet proved, and it seems sensible to hold drift rates to the levels indicated.

The uncertainty of the altitude of the apparent Mars limb has a range of values corresponding to various atmospheric models. These range from somewhat optimistic to a worst case assumption about luminance nonuniformity coupled to a worst case assumption about the altitude of the apparent limb. The *Mariner IV* data

probably will permit some reduction of the upper bound on this error.

e. Constraints on other equipment. Several constraints and requirements will need to be imposed on other equipment if the approach guidance system is to achieve the proposed performance level.

The Canopus tracker equivalent angle noise will have to be held to the present level of 0.03 deg peak-to-peak.

Calibration of the Sun and Canopus sensor error output voltage versus error angle will be required, so that the position within the limit cycle can be obtained with a peak error of 0.03 deg. The concern is not with null offsets and scale factor changes, but only with the nonlinearities. It is expected that curves run during normal functional testing will be adequate for this purpose.

Calibration of the analog telemetry channels used for the Sun and Canopus error signals will be required, so that the peak error will be less than 3% of full scale. This is normally done.

Drifts of the Sun and Canopus sensors will need to be less than 0.001 deg over a one-day period. This is believed to be within the capability of present instruments.

The Sun sensor power supplies will need a stability of 0.1% over a one-day period.

The mechanical mounting of the Sun sensors, Canopus sensor, and planet approach tracker must hold relative motion between the different instruments to less than 0.001 deg over a one-day period. This will probably require mounting of these instruments on a common base.

The analog telemetry channels will need a stability of 0.1% over a one-day period.

The last three items appear to be the only ones requiring some action. Even here there is a possibility that errors of these types can be largely separated out of the data during ground computation.

2. The Design of Autopilot Systems for Liquid Injection Thrust Vector Control (LITVC) of Spacecraft Retromotors

a. Introduction. The use of a solid propellant retromotor for the Mars orbit insertion of the *Voyager* spacecraft is receiving serious consideration. The velocity increment required is in the range of 8600 ft/sec. In order to maintain the spatial orientation of the motor thrust axis an active autopilot system is required. One method of controlling the motor thrust direction is the controlled injection of a liquid into the exhaust stream of the motor. The vaporization and decomposition of the liquid injectant modifies the pressure profiles within the motor exit cone and results in a controllable deflection of the effective thrust vector. Two-axis control is achieved by the use of four injectors with individual flow control valves equally spaced around the exit cone of the motor. The magnitude of the thrust deflection is proportional to the injectant fluid flow rate, which is controlled by the flow control valves in response to command signals from the autopilot amplifier. Since this propulsion unit provides only pitch-and-yaw control, roll control must be provided by an auxiliary system and is not considered in this report.

For the purpose of analysis, it has been necessary to assume order-of-magnitude numbers for the structural characteristics of the vehicle. Typical center-of-gravity (cg) errors were estimated on the basis of experience with the *Ranger* and *Mariner* spacecraft. While the required gain of the autopilot will depend upon the magnitude of the spacecraft inertia and the force moment arms, the interrelationships presented in the analysis will apply to any spacecraft of this general class.

b. System description. The system is required to overcome vehicle disturbance torques caused by misalignment of the motor with respect to the center of gravity and by resonances of the spacecraft structure. It is also required to null out small initial spacecraft pointing errors which are due to the deadband characteristics of the cruise attitude-control system.

The basic elements of a single-axis autopilot system are shown in the block diagram of Fig. 3. The spacecraft position error is sensed by a single-axis floated gyroscope which, in conjunction with the autopilot amplifier and compensation network, controls the flow through the injector valves. Two types of gyros have been considered for the system. The low damping rate integrating gyro of the type used in the *Ranger* and *Mariner* systems is unsatisfactory for this system, as will be explained later in this report. The gyro best suited for this system is a high-damped integrating gyro with position gain H/D, between 0.2 and 2.5. The disadvantage of the heater control required for this gyro is outweighed by the elimination of the rebalance amplifier and integrating capacitors associated with the low-damping gyro. Rate feedback required

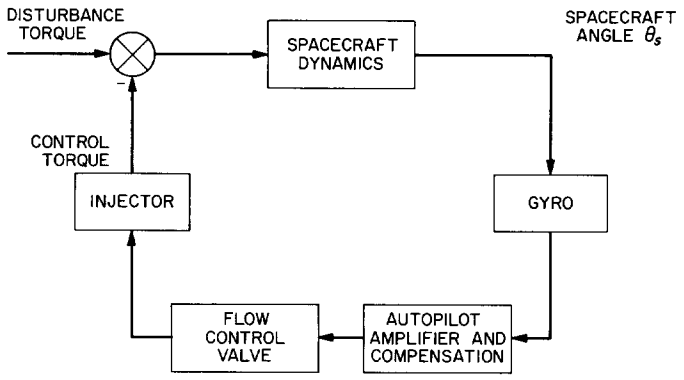

Fig. 3. Autopilot system

for servo compensation is obtained by the use of a lead-lag network in the autopilot amplifier.

The flow of injectant fluid into the exhaust cone is controlled by an electrically operated flow-control valve. The valve pintle is designed so that the fluid flow is proportional to the input current. The side force on the rocket motor is proportional to the injectant flow rate for the small thrust vector deflections required of this system. The side-force variation is less than 5% over the operating thrust range of the main retromotor. Preliminary spacecraft layouts indicate that the use of rigid solar panels will maintain all the structural resonant frequencies above 20 cps at 1 to 2% of critical damping. The resonance of the retromotor attachment is between 30 and 40 cycles. The uncertainty of the center-of-gravity location is ± 0.2 in. for the spacecraft and ± 0.04 in. for the motor and propellant. The distance from the point of application of injector side force to the center of gravity is 16 in.

The force diagram of Fig. 4 illustrates the torques on the vehicle due to thrust misalignments and the autopilot restoring torque. The error between the line of the undeflected thrust vector and the system center of gravity is the combination of two independent errors as shown. The motor thrust offset is the distance between the thrust axis and the nominal center of gravity on the motor centerline. The center-of-gravity error is the distance from the motor centerline to the actual center of gravity. The undeflected thrust vector in conjunction with the above errors produces a disturbance torque which tends to rotate the vehicle. The autopilot senses the rotation and, by controlling the secondary injectors, produces a side force to neutralize the disturbance torque.

The inertial reference line, indicated I in the diagram, represents the desired spatial orientation of the thrust vector. The net force on the vehicle is resolved into

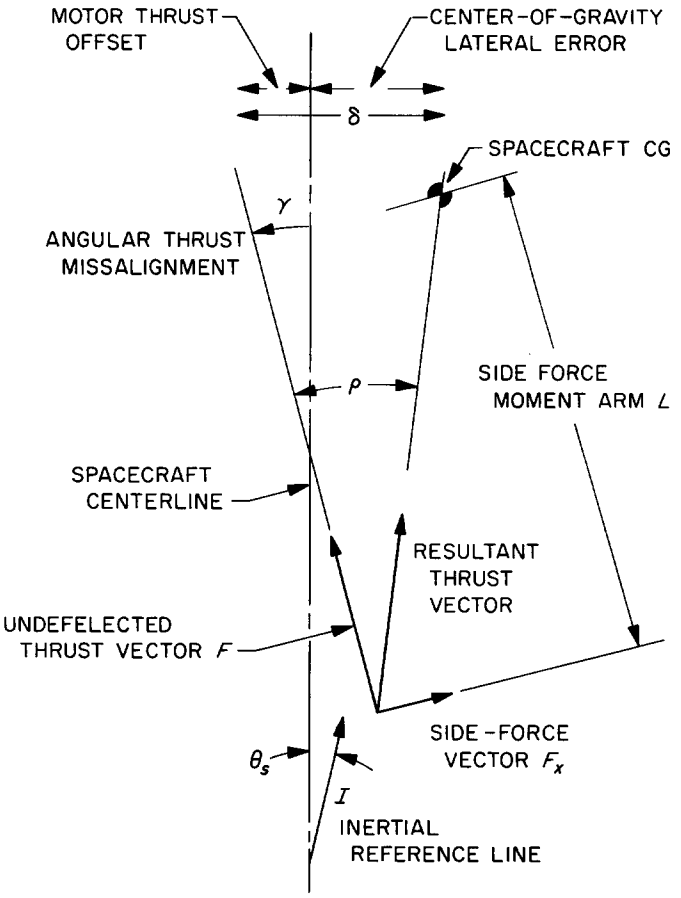

Fig. 4. Spacecraft force diagram

orthogonal components referenced to the I direction. The component normal to I gives rise to a velocity error and is referred to as the transverse force error F_T. The spacecraft attitude error θ_s is the angle between the spacecraft centerline and the I direction. It is seen that the undeflected thrust vector makes an angle $\theta_s + \gamma$ with the I direction and the transverse force is

$$F_T = F \sin(\theta_s + \gamma) + F_x \cos(\theta_s + \gamma)$$

or

$$F_T = F(\theta_s + \gamma) + F_x \qquad (1)$$

since $\theta_s + \gamma$ is less than 1 deg.

It is seen that while the angular thrust misalignment γ, does not give rise to any disturbance torque, it contributes to the system error F_T. Since γ produces an error independent of center-of-gravity errors, structural characteristics and autopilot performance, and has no interaction with the autopilot system, the remainder of this report

will be concerned with errors exclusive of γ. Rewriting Eq. (1) for $\gamma = 0$

$$F_T = F\theta_s + F_x \tag{2}$$

c. System analysis. The behavior of the system is analyzed with the aid of the functional block diagram of Fig. 5. It is seen from the force diagram that the disturbance and control torques on the vehicle are $F\sigma$ and F_xL, respectively. Their sum represents the net torque accelerating the inertia of the vehicle. At first the vehicle will be treated as a rigid body with moment of inertia J and the nonrigid body dynamics will be introduced later. For simplicity the DC gain of the gyro and compensation is made 1 rad/rad, and the actuator gain is K_A lb/rad. The dynamic response of the actuator and injector is approximated by the second-order poles $(S \pm S_a)^2$ with a natural frequency of 30 cps and 50% critical damping.

The two components of transverse force can be determined from the block diagram by equating the net steady-state torque to zero.

$$F\sigma - K_AL\theta_s = 0$$

or

$$\theta_s = \frac{F\sigma}{K_AL} \tag{3}$$

and

$$F_x = \frac{F\sigma}{L} \tag{4}$$

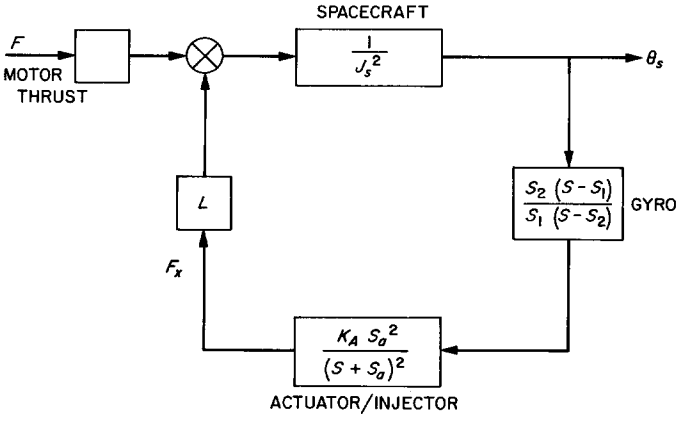

Fig. 5. Autopilot functions

Substituting $\rho = \sigma/L$ Eqs. (2), (3), and (4) yield

$$\frac{F_T}{F} = \rho\left(\frac{F}{K_A} + 1\right) \tag{5}$$

which is a measure of the pointing error of the system. This expression is a different form from the pointing error equation for the jet vane and gimbaled systems where

$$\frac{F_T}{F} = \rho\left(\frac{1}{K_\beta} + 1\right) \tag{6}$$

In those systems K_β represents the angular deflection of the thrust vector per unit spacecraft angle and is expressed in radians/radian. The control moment is then proportional to the motor thrust and F is a factor in the loop gain expression. In the secondary injection system the control moment and loop gain are independent of the motor thrust F, and herein lies the difference between Eqs. (5) and (6).

Eq. (5) is a convenient figure of merit of the system, but the determination of the actual transverse velocity error is complicated slightly by the fact that the motor thrust, center of gravity, and vehicle mass all change during the burning time. The center-of-gravity error ρ, is dependent upon the respective errors for the rocket propellant and the spacecraft bus.

$$\rho = \frac{\sigma_P M_P + \sigma_B M_B}{L\,(M_P + M_B)}$$

ρ = composite angular cg error

where

σ_p = cg uncertainty of propellant

σ_B = cg uncertainty of bus

M_P = mass of propellant

M_B = mass of bus less propellant

L = moment arm of injectors

or

$$\rho\,(t) = \frac{M_B}{M\,(t)}\,(\rho_B - \rho_P) + \rho_P \tag{7}$$

where

$\rho(t)$ = composite angular cg error at time t

$M(t)$ = total mass at time t

$\rho_B = \sigma_B/L$ = constant

$\rho_P = \sigma_P/L$ = constant

The system mass $M(t)$ can be determined from the thrust-time characteristic since

$$M(t) = M_0 - \frac{1}{gI_s}\int_0^t F(t)\,dt \qquad (8)$$

where

M_0 = system mass at ignition

I_s = specific impulse of the propellant in seconds

$F(t)$ = thrust at time t

Fig. 6 represents the analog computer simulation of Eqs. (5), (7), and (8) with $F(t)$ as the independent variable. Figs. 7 and 8 are the computer solutions for ρ, F_x, θ_s, and V_T for values of K_A of 28,000 and 140,000 lb/rad. With the larger value of K_A, the F/K_A term in Eq. (5) becomes negligible, and the error is simply proportional to the cg error ρ.

d. System stability. The importance of the autopilot gain K_A in minimizing velocity errors is apparent from the preceding section. To maintain low errors, it is desirable to make K_A between 3 and 10 times the motor thrust F. For the 14,000-lb maximum thrust of the system under consideration this corresponds to 42,000 to 140,000 lb/rad. The initial moment of inertia of the vehicle is estimated at 930 slug-ft² and the decrease due to propellant depletion is 180 slug-ft². With the moment arm of 1.36 ft the required loop gain K_AL/J is between 250 and 61 sec^{-2}.

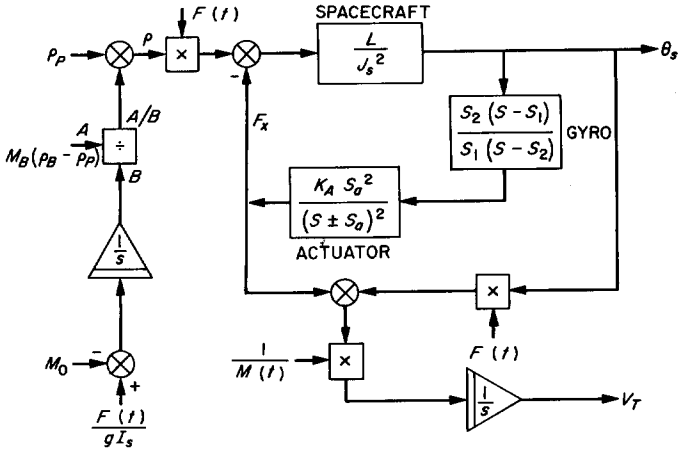

Fig. 6. Analog computer determination of V_T

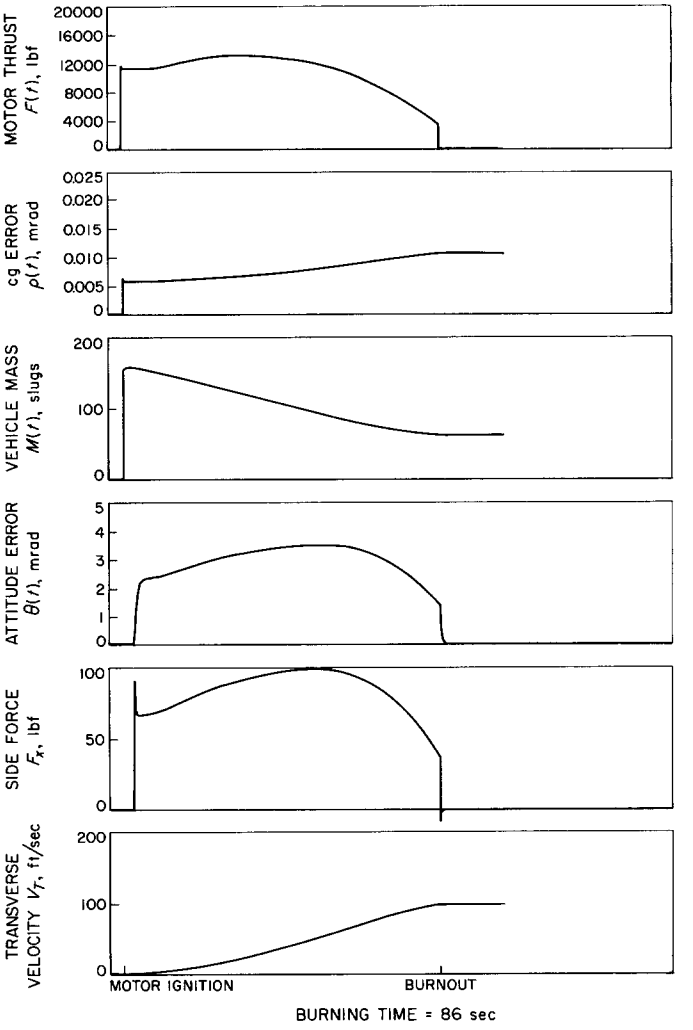

Fig. 7. Computer solution for transverse velocity error, autopilot gain K_A = 28,000 lb/rad

The secondary fluid injectors are approximated by a second-order system with a 30-cycle natural frequency and 50% damping. The low-damping rate-integrating gyro of the type used on the *Ranger* and *Mariner* spacecraft is represented by a 6.5-cycle second-order equation with 30% damping and a real zero corresponding to the rate gain term. The root locus diagram of this system is shown in Fig. 9. As an extreme case the real zero was located at

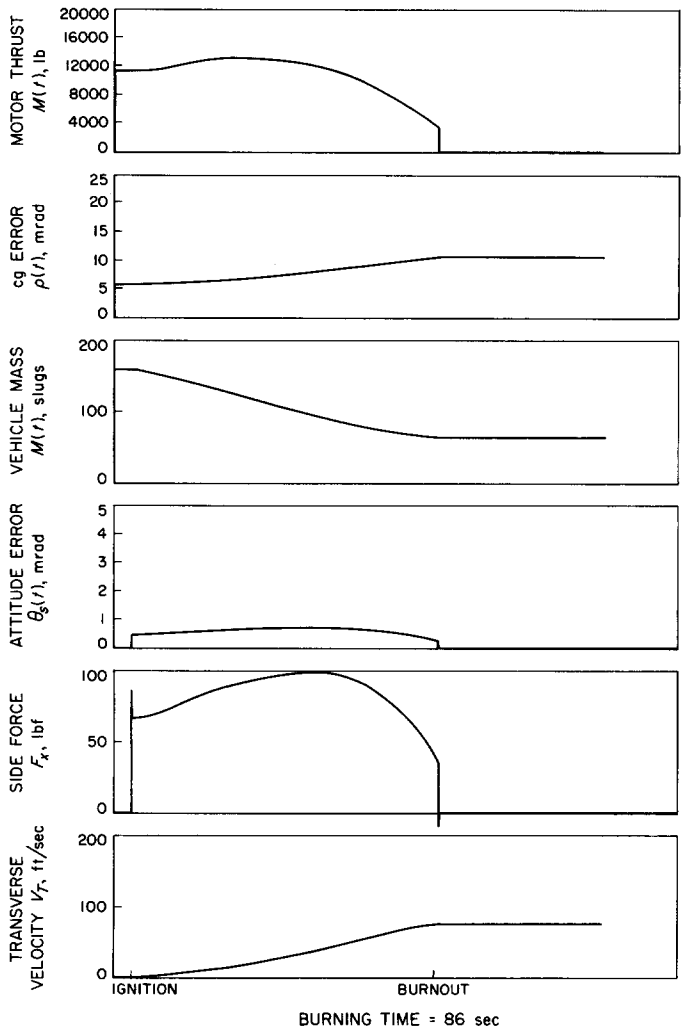

Fig. 8. Transverse velocity error K_A = 140,000 lb/rad

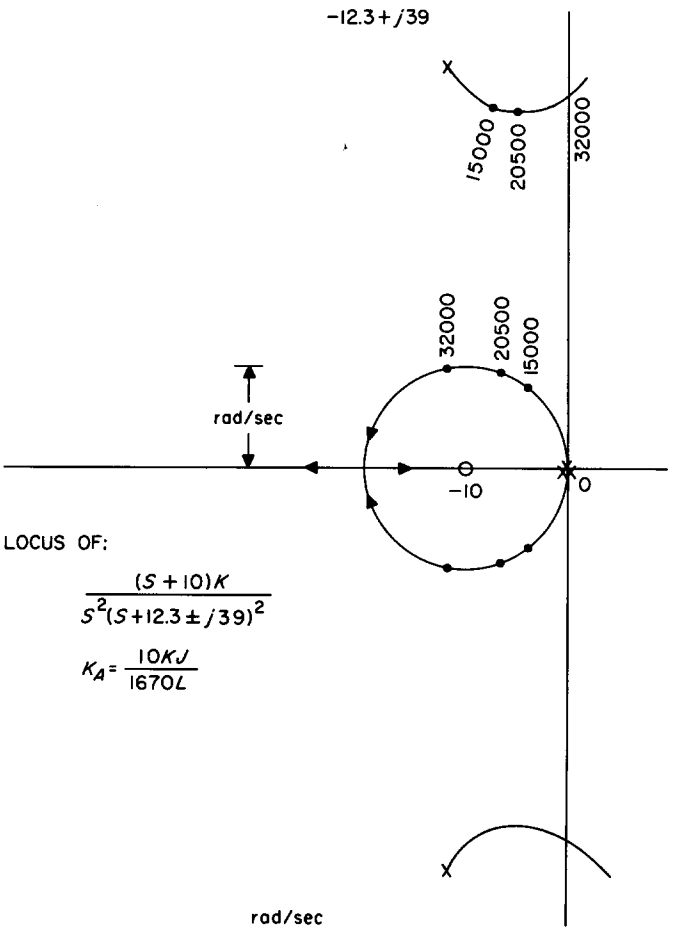

Fig. 9. Approximate root locus of system with closed loop gyro

-10 sec^{-1}. The maximum allowable gain is determined on the basis of a 12-db gain margin on the locus from the complex poles. This corresponds to an AC gain of 8000 and a K_A of 35,000 lb/rad. This low value of K_A is not only marginal from velocity error considerations, but the resulting closed-loop poles emanating from the origin have less than 30% damping. Moving the zero out beyond -10 sec^{-1} will allow a higher gain, but it will also have the adverse effect of reducing the damping of the poles from the origin, since they move out along a circle of increased radius. For this reason this type of gyro is considered marginal for the application and is not considered further.

A more desirable gyro for this application is the high-damping integrating gyro, also known as the wide-angle gyro. This device is characterized by a very low-position gain H/D, and is used as a position sensor. The transfer function of the gyro is of the form

$$\frac{V_{out}}{\theta_{in}} = K\frac{H}{D(\tau s + 1)} \tag{9}$$

where τ is the J/D time constant of the precession axis and is between 0.2 and 2.5 msec for the system under consideration. The system is compensated by the use of a lead-lag network with an alpha of 10, as shown in the root locus diagram of Fig. 10. The pole and zero frequencies are adjusted to provide maximum damping at a gain corresponding to 150,000 lb/rad. Comparison of the root loci of Figs. 7 and 8 shows that the high damping gyro enables a four times increase in DC gain, along with increased damping of the dominant poles and a wider gain margin. Fig. 10 represents the highest value of K_A one would consider, since it represents a F/K_A term of 0.10 in Eq. (5). The transient response of this system is

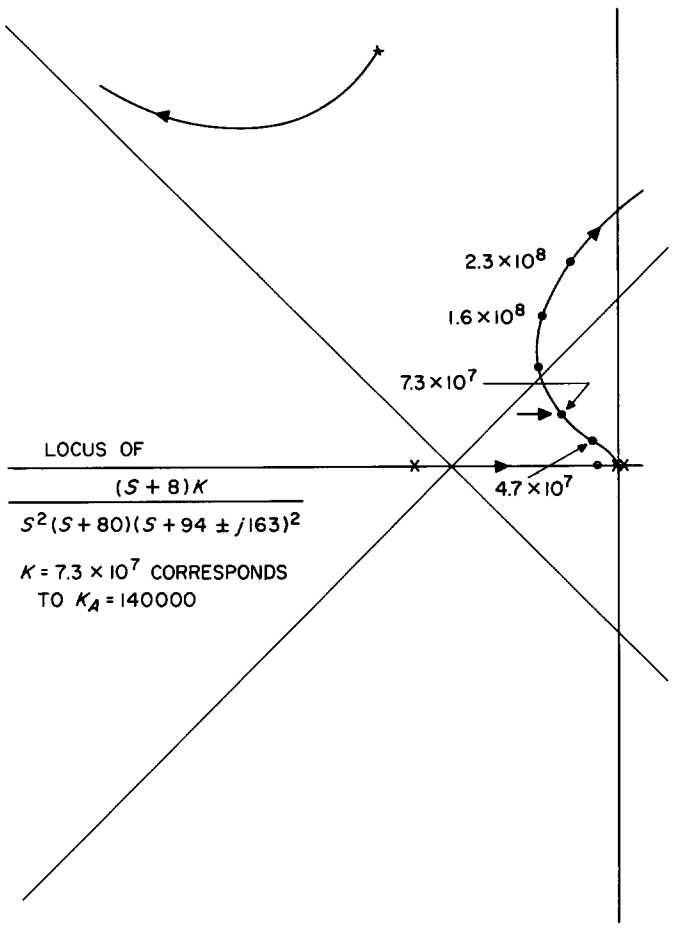

Fig. 10. Root locus of system with position gyro

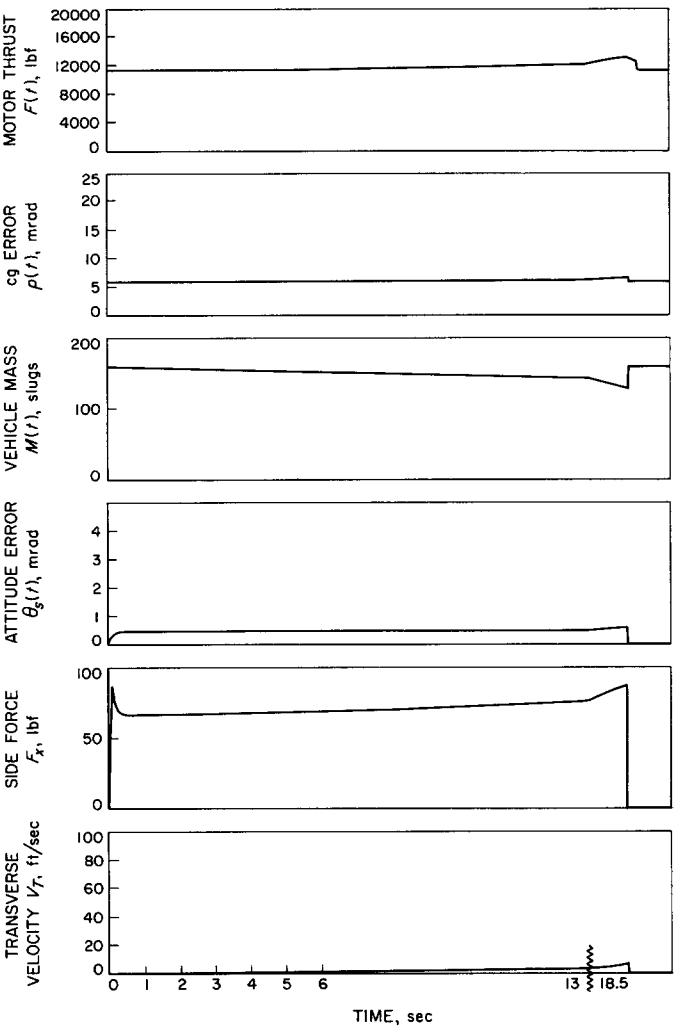

Fig. 11. Transient response of system with high-damping gyro, K_A = 140,000 lb/rad

shown in Fig. 11, and the performance over the full burning time is shown in Fig. 8.

e. Structural considerations. Resonances of structural appendages such as solar panels, antennas, and science instrument booms introduce complex pole-zero combinations into the spacecraft transfer function. The characteristic transfer function is of the form

$$\frac{\theta}{T} = \frac{S^2 + 2\zeta\omega_n S + \omega_n^2}{J_B S^2\left(S^2 + 2\dfrac{J_B + J_R}{J_B}\zeta\omega_n S + \dfrac{J_B + J_R}{J_B}\omega_n^2\right)} \qquad (10)$$

where

ω_n = resonant frequency of the structural member

ζ = damping ratio of the structural member

J_B = moment of inertia of the bus

J_R = moment of inertia of the resonant member about the cg of the bus

In the limit as s approaches zero, Eq. (10) becomes equal to $1/(J_B + J_R)S^2$ which is the rigid body approximation used previously.

Three useful relationships between the zeros and the poles can be derived from Eq. (10)

$$\frac{\omega_P}{\omega_Z} = \sqrt{\frac{J_R + J_B}{J_B}}$$

$$\frac{\sigma_P}{\sigma_Z} = \frac{J_R + J_B}{J_B} \qquad (11)$$

$$\frac{\zeta_P}{\zeta_Z} = \sqrt{\frac{J_R + J_B}{J_B}}$$

where

ω is the natural frequency of the pole or zero

σ is the real part of the pole or zero

ζ is the damping ratio

and subscripts $_p$ and $_z$ refer to the poles and zeros, respectively.

The effect of structures resonances on the system can be determined with the root locus plot of Fig. 12 which shows the root loci for the system with a resonant structure. The root locus from the structures poles lies within the left-half plane and connects the pole and zero associated with the resonance. However, as the resonant frequency of the structure is increased, there is a point at which the locus crosses into the right-half plane and the system becomes unstable. This occurs when the total phase contribution of the poles and zeros excluding those associated with the resonance exceeds 180 deg and the angle of departure of the locus becomes less than +90 deg.

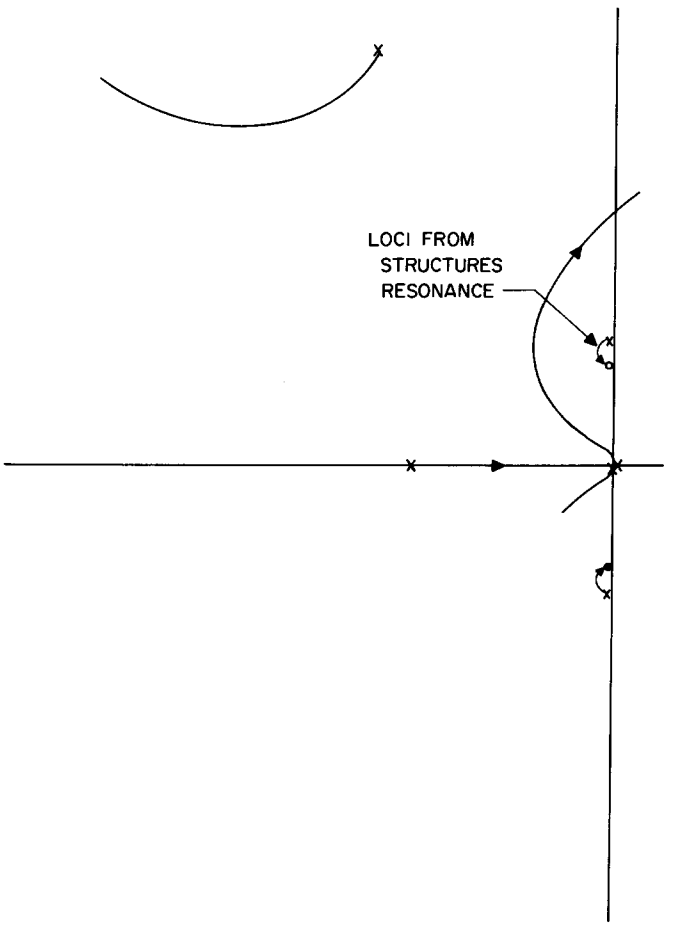

Fig. 12. Root locus of autopilot system with structures resonance at 9.5 cps

This condition exists over a frequency band for which the net phase, as described above, is between 180 and 360 deg. Structures resonances can be tolerated in this critical region, provided that the structural damping is high enough so that the closed-loop poles still lie within the left-half plane. While the exact solution for the required damping is complicated by the zero associated with the structures pole, several useful approximations can be made to simplify the problem.

Consider the point where the locus from the structures resonance pole crosses the imaginary axis. At this point the loop gain of the system, including the effect of the resonant structure, equals −1. Then the gain associated with the structure must be the reciprocal of the gain of the system exclusive of the structures resonance. As a conservative estimate, it can be assumed that the locus intersects the imaginary axis at the frequency of the structures pole. Then the maximum allowable structural gain, as a function of resonant frequency, can be determined from a Bode plot of the control system gain. It is seen that for any structures resonance satisfying this criteria the resulting closed-loop poles are in the left-half plane, and the system is stable. Even though the gain is less than 20 db down from 0 db at frequencies near the lower end of the critical region, very little structures damping may be required, depending upon the proximity of the zero to the pole. For example, a structure having an inertia moment of one fourth that of the bus, a resonant frequency of 18 cycles and 2% damping, has zeros at $-2.26 \pm j113$ and poles at $-2.8 \pm j127$. The corresponding gain at resonance is 4.50, which is just within the gain margin of the system.

Referring again to Fig. 12, it is seen that, as the structures resonant frequency is reduced, there is a point at which the loci emanating from the origin terminate on the zeros of the resonance, and the loci from the poles of the resonance migrate away from the zeros. This greatly reduces the damping of the dominant closed-loop poles and results in a very unsatisfactory system. This condition is avoided by maintaining the structural resonances above 1.6 cycles. The structural resonance criteria are summarized in Fig. 13, which shows the critical frequency range and the amplitude limit.

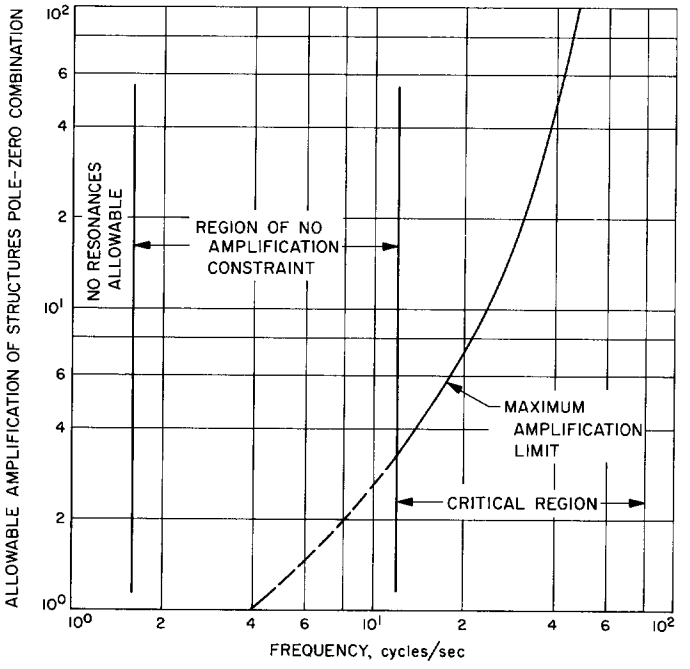

Fig. 13. Structural resonance criteria

f. System performance. The transient responses of a system including the aforementioned 18-cycle resonant structure, side force limiting at 200 lb and a nominal cg error are shown in Fig. 14. The parameters of the system are listed in Table 2.

The system of Fig. 14 has the same autopilot gain K_A as the system of Fig. 8, so the steady-state velocity errors should be comparable. Since Fig. 14 shows negligible velocity error built up during the transient response, the velocity error of 76 ft/sec of Fig. 8 may be used as typical of the system. This error divided by the 8600 ft/sec velocity increment of the retromotor corresponds to an effective system pointing error of 9 mrad.

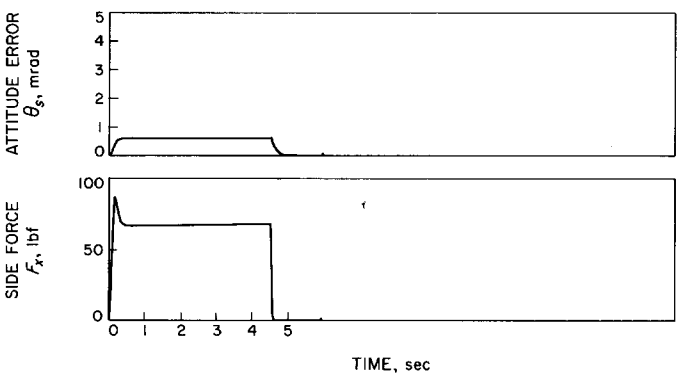

Fig. 14. Transient response of system, with structural resonance, K_A = 140,000 lb/rad

Table 2. List of parameters used in analysis

Symbol	*Parameter*	*Value*
ρ_B	Angular cg error of bus	10.3 mrad
ρ_P	Angular cg error of propellant	2.5 mrad
L	Side force moment arm	1.36 ft
M_0	Vehicle mass at ignition	160 slugs
I_s	Specific impulse of propellant	308 sec
J	Moment of inertia of vehicle	930 slug-ft²
K_A	Autopilot side force gain	140,00 lb/rad[a]
S_Z	Complex frequency of zeros associated with resonant structure	$-2.26 \pm j113$
S_P	Complex frequency of poles associated with resonant structure	$-2.8 \pm j127$
J_R	Moment of inertia of the resonant member about the cg of the bus	186 slug-ft²
J_B	Moment of inertia of the bus less the resonant member	744 slug-ft²
ω_n	Natural frequency of the resonant member	18 cps
ζ	Damping ratio of resonant member	0.02 critical
S_a	Complex frequency of actuator poles	$-95 \pm j165$ rad/sec
S_1	Complex frequency of the zero of the compensation network	-8 rad/sec
S_2	Complex frequency of the pole of the compensation network	-80 rad/sec

[a]In Figs. 7 and 9, K_A = 28,000 lb/rad

3. Power Systems

a. Spacecraft power. The task assignments in support of the *Voyager* Project have been reviewed and revised to place more emphasis on those areas of power system

design that are of immediate *Voyager* interest. These task assignments have two main purposes:

(1) To investigate in detail those areas of power system design of possible adaptation to the *Voyager* mission.

(2) To provide a reservoir of information on power system components and technology.

To date the following subtasks have been started and interim reports issued:

(1) A detailed review of the *Mariner C* power system design in order to improve design for *Voyager*.

(2) A parametric analysis of the effects of power subsystem frequency, voltage regulation, input voltage range, output power, and voltage on such parameters as weight, reliability, and efficiency.

(3) An analysis of the problem of providing increased power conditioning equipment reliability using redundancy, switching of loads, fault sensing, and clearing, etc.

(4) An analytical comparison of the advantages and disadvantages of down-regulating switched regulators and booster regulators.

(5) The acquisition and correlation of parametric performance data on silver-zinc, silver cadmium, and nickel cadmium batteries.

(6) Analysis of parametric performance data on new solar cell types.

(7) An investigation of the advantages and disadvantages of using a *Mariner C* power system mechanization method for the *Voyager* bus.

(8) A review of the methods used in establishing power subsystem design margins and recommendations for margin allotments in the *Voyager* program.

(9) Parametric design, on a functional block level, of power systems for various power levels.

Work on all the above subtasks is proceeding satisfactorily.

User power requirement inputs for the *Voyager* spacecraft are being received from the subsystems concerned and are being assembled into matrices and power profiles for the various modes under consideration. The information gained from these matrices will be used to generate power system functional block diagrams.

A preliminary block diagram and a functional description have been generated from the information received and will be included in the revised *Voyager* spacecraft baseline design.

The power subsystem matrices assembled to date indicate that the spacecraft power demand, and therefore the power sources, have nearly doubled in size, compared with that of the original baseline.

b. Capsule power. A power profile and functional mechanization based on the first estimate of each subsystem's power requirement have been issued. The refinement of each subsystem's power requirement and overall sequencing for the "out-of-orbit" mode is continuing. The preliminary power profile and system mechanization have been used in a tradeoff study between a solar panel battery and a battery-only power source for the out-of-orbit mode.

4. Sterilizable Battery

a. Development of separators for sterilizable batteries. The development of a separator material capable of functioning satisfactorily in the Ag-Zn battery after heat sterilization, is continuing. The contract with Radiation Applications, Inc., has yielded two materials which have passed the preliminary testing phase and are now being evaluated further. The materials produced under the contract with the Narmco Division, Whittaker Corp., are thermally and chemically stable but are not usable as separators, due to their high resistivities.

JPL Contract 951015 with Radiation Applications, Inc. Under this contract, which has ended, fifty-one materials were prepared and tested, the final testing phase being electrical capacity measurements of cells constructed from sterilized materials. Cells made from seven materials had capacities greater than 90% after five complete cycles, and two of these have been produced in larger quantities for more extensive cell testing. One of these materials was made by a crosslinking procedure using an electron beam irradiation to a 70-mrad level followed by grafting with acrylic acid using irradiation from a Co^{60} source. The other material was made by a crosslinking procedure using divinylbenzene and a Co^{60} source, followed by grafting with acrylic acid. More extensive testing is being done by the Electric Storage Battery Co. and by JPL.

JPL Contract 951091 with Narmco Division, Whittaker Corporation. This contract, begun in June 1965, was for the investigation of new thermostable polymers as

sources for separator materials. The eight polymers to be synthesized were polybenzimidazoles, polybenzothiazoles, polybenzoxazoles, and polyquinoxalines. Six of these were prepared, and the polymers and films made from them have been characterized and evaluated for chemical and thermal stability. The chemical and physical properties of the film fabricated from poly-2,2′-(octamethylene-)5, 5′ bibenzimidazole were superior, and preparative modifications are being made to improve the resistivity value. The effort of the contract will be centered on the development of this polybenzimidazole and the evaluation of poly-2,2′-(p,p′-oxybisphenylene)-7,7′-oxybisquinoxaline.

b. Research and development of the heat sterilizable Ag-Zn battery. A research and development contract was awarded to the Electric Storage Battery Co., in September 1965 to study, develop, fabricate, and test sealed Ag-Zn and Ag-Cd secondary batteries capable of functioning satisfactorily following heat sterilization, high impact, and vibration. The contract includes electrochemical studies on electrodes, electrolyte solutions and separators, chemical and physical studies of case materials, and the design and testing of cells of both the Ag-Zn and Ag-Cd systems. The testing of two promising plastics for cells, polyphenylene oxide and polyphenylsulfone, has begun. Preliminary cell designs are being considered, and stress analyses associated with certain cell designs have been made.

C. Propulsion

1. Monopropellant-Hydrazine Showerhead Injector Tests With Spontaneous Catalyst

During the past two years, monopropellant-hydrazine rocket engine and gas generator testing programs have revealed a problem associated with the use of spontaneous catalyst beds (Refs. 1, 2, and 3). A chamber pressure disturbance occurs shortly after ignition, usually within 1 to 10 sec, depending upon injector and catalyst bed configurations. The disturbance appears as a transient pressure excursion, or spike, with a magnitude of about 170% of steady-state chamber pressure p_c, as measured by a Taber transducer and recorded on an oscillograph. It has been hypothesized that the pressure disturbance occurs when the primary reaction zone, which starts at the lower end of the catalyst bed, undergoes a rapid shift to the top portion of the catalyst bed. The liquid phase contained in the top section of the bed is heated by conduction and recirculation until it undergoes a rapid vaporization and chemical reaction with an associated change in specific volume, which results in a rapid pressure rise, or spike. The reaction zone location is detected by catalyst-bed thermocouple measurements, as well as color changes in the chamber wall.

As an extension of the previously reported work on the chamber pressure spike problem, new injector and catalyst bed configurations have been studied. A showerhead injector was designed, fabricated, and mated with a modified *Mariner C* flanged-test chamber as shown in Fig. 15. The injector produces 73 small discrete streams (0.010-in. D) which impinge on the top of the catalyst bed. The orifice configuration of the injector plate may be seen in Fig. 16. This is a radical departure from earlier injector designs which utilized four or five swirl-type atomizing nozzles to distribute the fuel over the upper portion of the catalyst bed. The showerhead injector was designed for a hydrazine flow rate of 0.217 lbm/sec, with a corresponding pressure drop Δp of 130 psi across the 0.125-in. thick injector plate.

The first series of tests, which was conducted with the engine/injector combination shown in Fig. 15, was

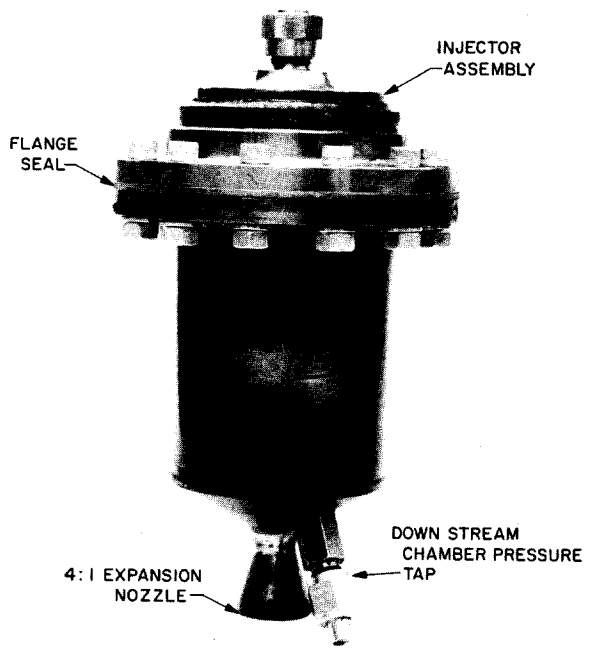

Fig. 15. Flanged test chamber with showerhead injector

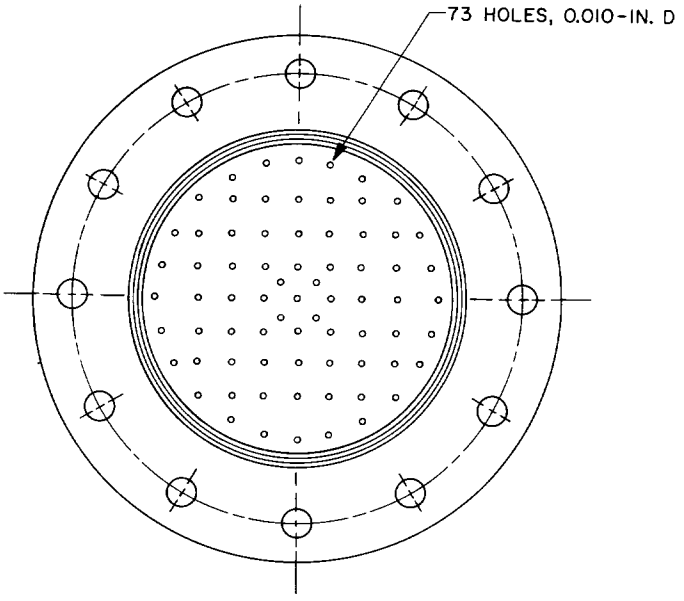

Fig. 16. Showerhead injector showing hole configuration in plate

intended to provide a limited examination of various bed-packing configurations. The test setup is shown schematically in Fig. 17, and the decomposition chamber installation is shown pictorially in Fig. 18.

The first two firings were made with a random-dense-packed (Ref. 4) bed of Shell 405 spontaneous catalyst

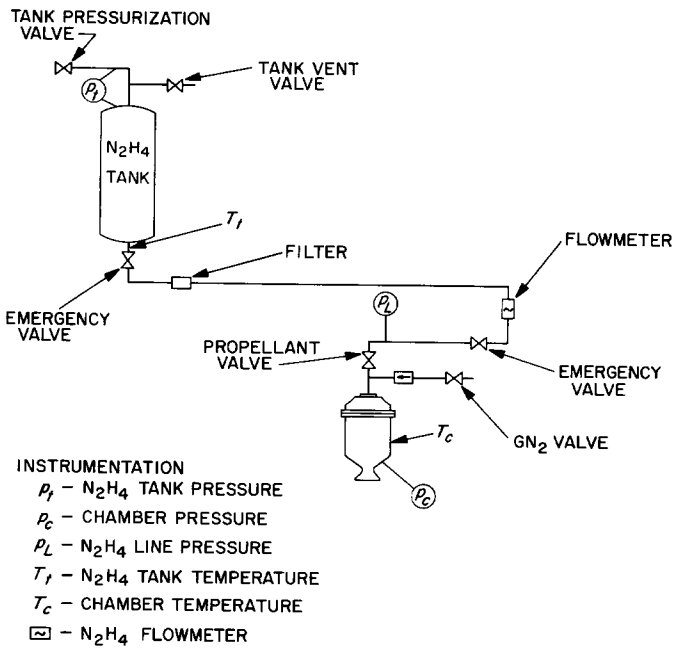

Fig. 17. Test setup

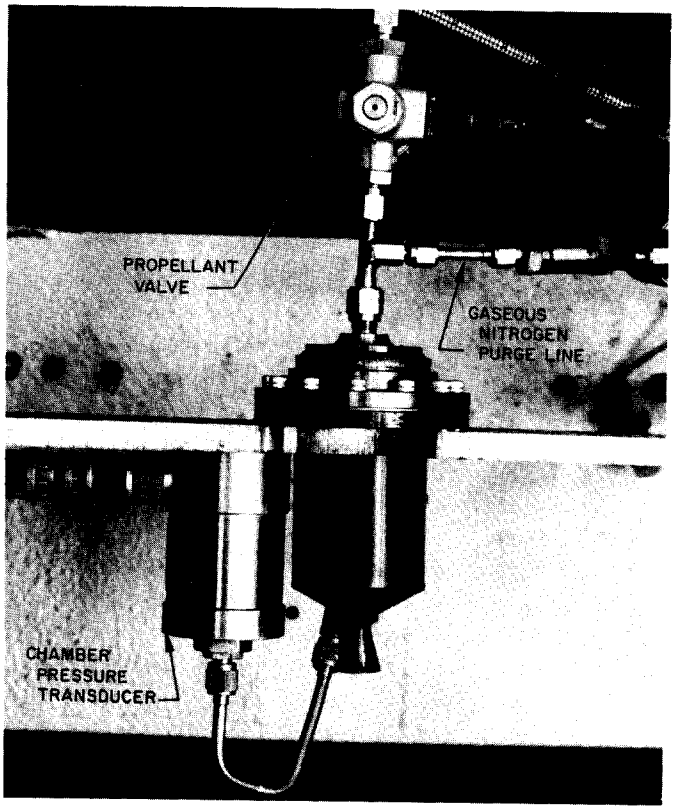

Fig. 18. Test chamber installation

pellets (⅛-in. long × ⅛-in. D.), as seen in Fig. 19. The catalyst which had been used in previous testing programs was packed into the chamber for the first test (No. 492, Table 3), and the unused catalyst was packed in the same manner for the second test (No. 493). The chamber pressure was rough in both tests (~190 psig ±8 psi) with no significant differences apparent. From the appearance of the chamber, and the thermocouple data, the primary reaction zone was at the bottom of the catalyst bed. Since this reaction zone location is least desirable, testing with this configuration was terminated.

Fig. 20 illustrates the chamber geometry for the third test (No. 494), utilizing a sleeve to contain the catalyst during assembly of the chamber. This technique was used to move the catalyst bed closer to the injector face. The data from this firing was similar to the previous two tests, except that the ignition delay[1] was longer, and the chamber pressure was considerably rougher (190 psig ±39 psi). The primary reaction zone appeared to be about in the middle of the chamber. The pressure drop

[1]Defined as time required from propellant valve opening to the attainment of 90% of steady-state chamber pressure (p_c).

Table 3. Results of catalyst bed configuration tests

Test No.	Bed configuration	Steady-state chamber pressure, p_c, psig	Steady-state chamber pressure, peak-to-peak, psi	Ignition delay time, msec	Chamber pressure spike occurrence	Catalyst bed pressure drop Δp_{cat}, psi
492	Fig. 19	189	16.0	94	No	12.0
493		192	10.2	124	No	16.0
494	Fig. 20	190	78.0	151	No	20.0
495	Fig. 21	168	2.6	167	No	40.0
496		162	2.6	136	No	48.0
497		152	3.0	135	No	56.0
498		160	4.5	150	No	68.0
516	Fig. 21[a]	180	2.4	975	Yes	20.0
517		180	5.1	1034	No	21.5
518	Fig. 21[b]	178	5.5	850	No	—
519		177	5.2	1750	Yes	—

[a]10 mesh used in lieu of 20 mesh.
[b]10-mesh layer was reduced to 0.5 in.

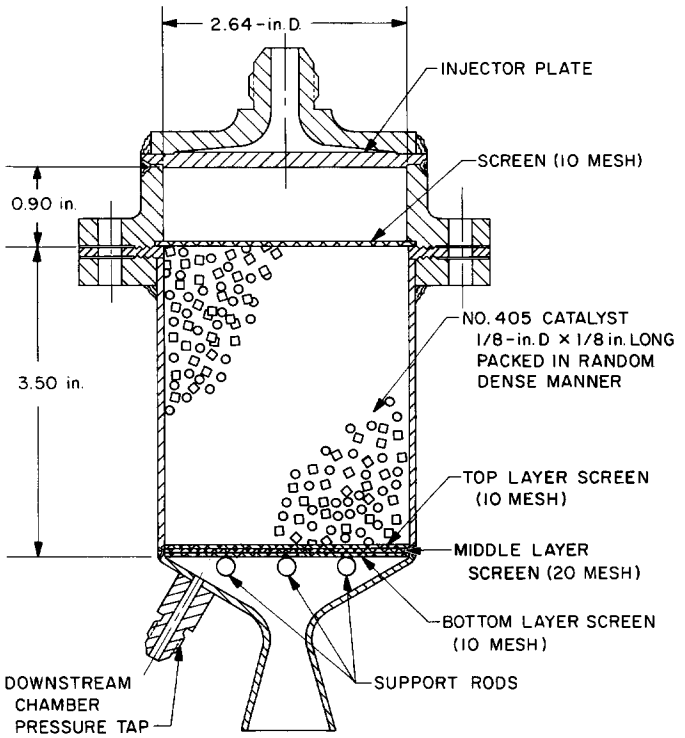

Fig. 19. Showerhead injector and test chamber cross section

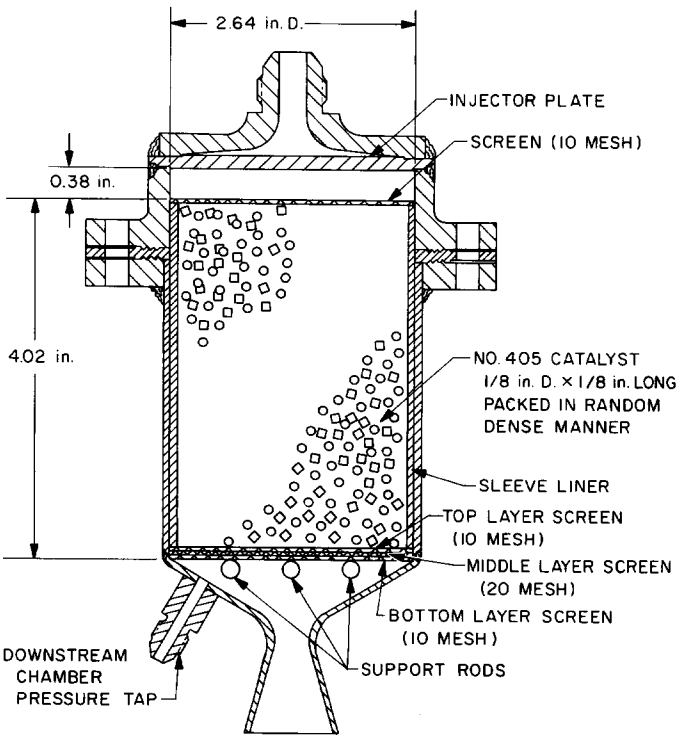

Fig. 20. Showerhead injector and test chamber with sleeve for catalyst

across the catalyst bed, Δp_{bed}, was comparable to the previous two firings, as shown in Table 3. This chamber packing technique was not explored further.

Because of the rough steady-state operation which occurred in the three previous tests, an attempt was made to increase the catalyst surface area exposed to the propellant. Four firings were made with the catalyst bed packed as shown in Fig. 21. A quantity of Shell 405 catalyst pellets was crushed with a mortar and pestle, and passed through a 20-mesh screen (Ref. 5). This layer of 20-mesh catalyst was packed on top of the ⅛-in.

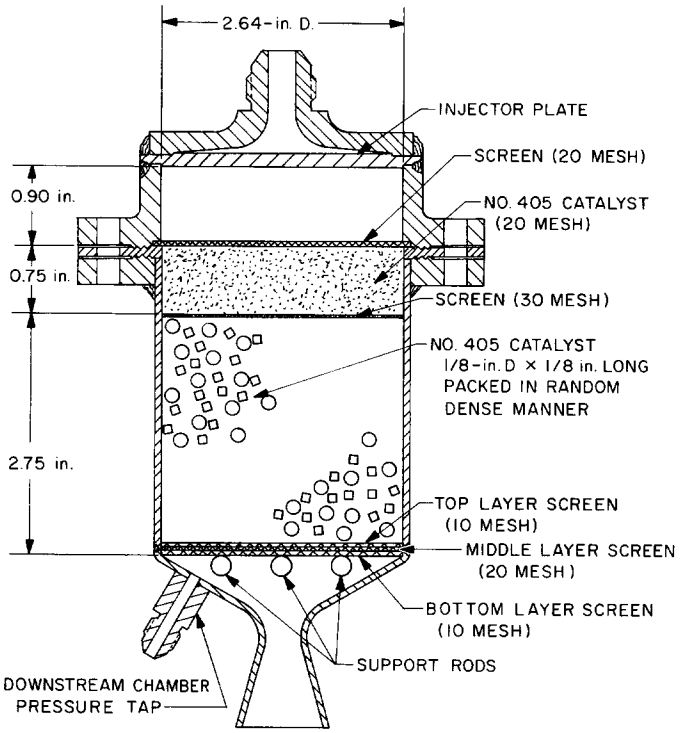
2.64-in. D.
INJECTOR PLATE
SCREEN (20 MESH)
NO. 405 CATALYST (20 MESH)
0.90 in.
0.75 in.
SCREEN (30 MESH)
NO. 405 CATALYST 1/8-in. D × 1/8 in. LONG PACKED IN RANDOM DENSE MANNER
2.75 in.
TOP LAYER SCREEN (10 MESH)
MIDDLE LAYER SCREEN (20 MESH)
BOTTOM LAYER SCREEN (10 MESH)
SUPPORT RODS
DOWNSTREAM CHAMBER PRESSURE TAP

Fig. 21. Showerhead injector and test chamber with 20-mesh catalyst

pellets, forming two layers within the chamber. The results of these four tests (Nos. 495–498) indicated that a very smooth chamber pressure could be obtained (maximum p_c deflection $\sim \pm 1.6$ psi), with moderate ignition delay times. However, the pressure drop across the bed, Δp_{bed}, did increase progressively from 40 psi in the first test to 68 psi in the fourth test. This indicated that the bed was packed during the firings. A visual inspection of the chamber was made after disassembly and the bed appeared to have a thin layer (0.1-in.) of powdered catalyst on top. The remaining 20-mesh layer had to be pried out in chunks. The chunks were not sintered and broke apart readily when handled. The ⅛-in. catalyst pellets were not changed physically.

Based on the information from the preceding tests (Nos. 495–498), subsequent tests were planned to determine the optimum catalyst bed geometry with a correspondingly low catalyst-bed pressure-drop Δp_{bed}. Only four firings have been completed at the time of this report. The bed geometry for the first two tests (Nos. 516 and 517) was the same as shown in Fig. 21, except that 10-mesh catalyst was used for the top layer in lieu of 20 mesh. A chamber pressure spike of about 376 psig occurred on the first firing within 0.200 sec from the time that the propellant valve opened. The ignition delay time was very long (0.975 sec), but the Δp_{bed} was only 20 psi. The second firing also had a long ignition delay, but the Δp_{bed} did not change appreciably. For the last two firings (Nos. 518 to 519), the catalyst bed was stratified as in the two previous tests, but the thickness of the 10-mesh catalyst layer was reduced to 0.5 in. The chamber pressure was smooth, but the ignition delay was longer. During the fourth firing, a chamber pressure spike was observed within 0.9 sec after the valve opening with a peak pressure of 300 psig.

It is evident from the data which are presented in Table 3 that an optimum stratified catalyst-bed configuration should be obtainable in which the pressure drop is reduced to an acceptable level, relatively low-ignition delay times are maintained, and pressure spikes are avoided. A considerable amount of work is yet to be done in defining the interrelation of parameters such as catalyst size, bed geometry, and possibly injector design.

References

1. Mattson, R. F., "Monopropellant-Hydrazine Investigation," *SPS 37-36*, Vol. II, Jet Propulsion Laboratory, California Institute of Technology, Pasadena, California, November 30, 1965.

2. Kocsis, J. D., "Gas Generator Development," *SPS 37-25*, Vol. IV, Jet Propulsion Laboratory, California Institute of Technology, Pasadena, California, February 29, 1964, pp. 100–101.

References (Cont'd)

3. Kocsis, J. D., "Gas Generator Development," *SPS 37-31*, Vol. IV, Jet Propulsion Laboratory, California Institute of Technology, Pasadena, California, February 28, 1965, pp. 197–201.

4. Grant, A. F., Jr., "Basic Factors Involved in the Design and Operation of Catalytic Monopropellant-Hydrazine Reaction Chambers," Report No. 20-77, Jet Propulsion Laboratory, Pasadena, California, December 21, 1954 (Confidential).

5. *Chemical Engineers' Handbook*, Third Edition, Section 15, McGraw-Hill Book Co., New York, N. Y., pp. 955.

III. Future Projects

A. Introduction

The JPL Future Projects Office is responsible for the direction, sponsorship, and, in cooperation with other technical areas of the Laboratory, origination of advanced mission and future project studies of interest and applicability to the Laboratory space program. The objective is to ensure the availability, when required, of preliminary technical information and plans for potential missions, including associated information on spacecraft systems, instrumentation, launch vehicle systems, resources, and schedule requirements. This preliminary information will be used to define specific flight mission projects and to provide general guidelines for the direction of Laboratory research and advanced development efforts. A summary or informative abstract of the results of each study will be presented in the *Space Programs Summary*, including, where appropriate, reference to the more detailed formal final report issued by the Future Projects Office.